Hydro-mechanical analysis of a surficial landslide triggered by artificial rainfall: the Ruedlingen field experiment

Sitarenios, P., Casini, F., Askarinejad, A. & Springman, S.

Hydro-mechanical analysis of a surficial landslide triggered by artificial rainfall: the Ruedlingen field experiment

Author 1
- **Panagiotis Sitarenios**, Lecturer in Civil Engineering - Geotechnics
- <u>Current Affiliation:</u> School of Energy, Construction and the Environment, Coventry University, Coventry, UK
- <u>Former Affiliation:</u> Department of Civil Engineering and Computer Science, University of Rome Tor Vergata, Rome, Italy
- https://orcid.org/0000-0002-7292-9500
- email: panagiotis.sitarenios@coventry.ac.uk

Author 2
- **Francesca Casini**, Associate Professor
- Department of Civil Engineering and Computer Science, University of Rome Tor Vergata, Rome, Italy
- https://orcid.org/0000-0001-7933-9055
- email: francesca.casini@uniroma2.it

Author 3
- **Amin Askarinejad**, Assistant Professor
- Faculty of Civil Engineering and Geosciences, TU Delft, The Netherlands
- https://orcid.org/0000-0002-7060-2141
- email: A.Askarinejad@tudelft.nl

Author 4
- **Sarah Springman**, Professor
- Institute for Geotechnical Engineering, ETH Zurich, Switzerland
- email: sarah.springman@igt.baug.ethz.ch

Corresponding author:
- **Panagiotis Sitarenios**, Lecturer in Civil Engineering - Geotechnics
- School of Energy, Construction and the Environment, Coventry University, Coventry, UK
- address: Sir John Laing bldg., Coventry, UK, CV1 5FB
- email: panagiotis.sitarenios@coventry.ac.uk
- tel: +44 (0) 2477 650 899

Abstract

This paper interprets the hydromechanical behaviour of a steep forested instrumented slope during an artificial rainfall event, which triggered a shallow slope failure fifteen hours after rainfall initiation. The soil's mechanical response has been simulated by coupled hydro-mechanical finite element analyses, using a critical state constitutive model that has been extended to unsaturated conditions. Failure occurs within a colluvium shallow soil cover, characterised as a silty sand of low plasticity. The hydraulic and mechanical parameters are calibrated, based on an extended set of experimental results, ranging from water retention curve measurements to triaxial stress path tests under both saturated and unsaturated conditions. Rainfall is simulated as a water flux at the soil surface and suitable boundary conditions account for the hydromechanical interaction between the soil cover and the underlying bedrock. The results are compared with field data of the mechanistic and the hydraulic responses up to failure and are found to provide a very satisfactory prediction. The study identifies water exfiltration from bedrock fissures as the main triggering agent, resulting in increased pore pressures along the soil - bedrock interface, reduced available shear strength and cause extensive plastic straining, leading to the formation and propagation of a failure surface.

List of notation

a tensile strength

b water retention model parameter (slope of the water retention curve)

c cohesion

e void ratio

k_{rel} relative permeability

k_{sat} saturated permeability

M slope of the critical state line

N_{iso} specific volume value (1+e) of the isotropic virgin compression line at p'=1kPa

n porosity

n_c CASM model (yield surface shape parameter)

n_0 reference porosity for the water retention model

P water retention model parameter (controls the air-entry value)

P_0 water retention model parameter (for void ratio dependence)

$p_0(s)$ apparent preconsolidation pressure

$p_0{}^*$ saturated preconsolidation pressure – hardening variable

p mean total stress

p' Bishop's mean skeleton stress

p^c reference pressure

p^t isotropic tensile strength

q deviatoric stress

r parameter controlling the evolution of virgin compressibility with suction

r_c CASM model (yield surface shape parameter)

S_r degree of saturation

$S_{r,res}$, $S_{r,max}$ residual and maximum degree of saturation

s suction ($s=u_a-u_w$)

t time

U_x, U_y, U_h, U_v x-axis, y-axis, horizontal and vertical displacement

u_a air pressure

u_w water pressure

w gravimetric water content

z depth from the slope surface

α water retention model parameter (air-entry value dependence on void ratio)

β parameter controlling the evolution of virgin compressibility with suction

δ_{ij} Kronecker delta

ε_q deviatoric strain

η stress obliquity

θ volumetric water content

κ	elastic compressibility
$\lambda, \lambda(s)$	saturated (for s=0) and unsaturated virgin compressibility
v	Poisson's ratio
σ_{ij}	total stress tensor
σ'_{ij}	Bishop's skeleton stress tensor
φ'	angle of internal friction

1. Introduction

Landslides are one of the most commonly occurring natural phenomena with consequences ranging from minor, to huge and devastating. Factors associated with topography, geological - geotechnical conditions, environmental – climatic factors and human activities can increase slope failure susceptibility. Landslides occur frequently in relatively steep topography in mountainous or hilly terrains (Rickli *et al.* 2008), while one of the most common triggering agents is rainfall (e.g., Caine (1980); Springman *et al.* (2003); Guzzetti *et al.* (2004); Cascini *et al.* (2008); Salciarini *et al.* (2012), Tang *et al.* (2018)). Accordingly, rainfall induced landslides, have attracted significant attention from researchers worldwide and numerous experimental (e.g., Wang & Sassa (2003), Take *et al.* (2004), Wu *et al.* (2015)) and numerical studies (e.g., Laloui *et al.* (2015), Lollino *et al.* (2016)) focus on studying the mechanisms associated with the failure of natural or artificial slopes during rainfall.

Rainfall induced landslides are the outcome of the progressive saturation of a surficial soil profile, which decreases the available shear strength and leads to the formation of a failure zone. The hydromechanical behaviour of the unsaturated soil layer plays a fundamental role in the approach to failure. Field experiments offer a comprehensive way to study such behaviour as a full scale "prototype", with relevant indicative studies including Harp *et al.* (1990), Ochiai *et al.* (2004) and Askarinejad *et al.* (2018). Most of these contributions emphasise the complexity of the mechanisms underlying rainfall induced slope instabilities, highlighting that apart from the mechanical and hydraulic characteristics of the unsaturated soil formations, additional factors pertain. These may include the existence of preferential water flow paths (e.g., fissures), vegetation (e.g., root reinforcement), the initial hydraulic field and its seasonal variations and the bedrock shape (e.g., Damiano *et al.* (2017), Lehmann *et al.* (2013), Askarinejad *et al.* (2014), Brönnimann *et al.* (2013), Ng *et al.* (2001)).

Numerical analyses can further supplement such studies by providing the means to assess and evaluate the field measurements and carry out parametric analyses (e.g., Rahardjo *et al.* (2007)). Coupled hydromechanical analyses with the Finite Element Method (FEM) are the most commonly utilised tool for the numerical investigation of rainfall induced slope instabilities (Leroueil 2001; Elia *et al.* 2017) because they facilitate a detailed simulation of the slope's complete loading history (e.g, consolidation, rainfall duration and intensity). Complex physical processes related to slope's saturation, including water flow under unsaturated conditions and the soil's water retention behaviour, can also be modelled. Moreover, they can be combined with advanced constitutive models extended to unsaturated conditions to reproduce the soil behaviour more accurately in the transition between saturated and unsaturated conditions, such as the swelling or collapse upon wetting and its dependence on the applied stress level, and the evolution of compressibility and of shear strength with wetting.

A set of 2D coupled hydromechanical analyses have been carried out with the finite element method computer software Code Bright (Olivella *et al.* 1996) to reproduce the behaviour monitored during the Ruedlingen field experiment (Askarinejad *et al.* 2012; Springman *et al.* 2012), where a steep silty slope was subjected to artificial rainfall leading to a shallow slope failure after 15 hours. Askarinejad *et al.* (2012b) report a set of different numerical studies to reproduce the experimentally observed behaviour, mainly including limit equilibrium calculations based on simplified geometries of an infinite slope and a 3D sliding block, supported by preliminary 2D uncoupled numerical simulations.

This paper advances previous work through coupled hydromechanical analyses of the soil cover, in order to evaluate the mechanical and hydraulic response of the slope, and

to explore whether such numerical analyses are capable of reproducing the pre-failure behaviour. The discussion focuses on the detailed modelling of the hydromechanical behaviour of the Ruedlingen soil. A critical state plasticity model for unsaturated soils is utilised and calibrated based on available experimental results. The investigation captures the field observations very well, both in terms of the mechanical and of the hydraulic behaviour and identifies water exfiltration from the bedrock as the main triggering agent. Parameters and assumptions about the slope's behaviour are varied within a parametric study.

2 Field Experiment

Two full scale field tests were performed to study the response of a steep forested slope subjected to artificial intense rainfall (Askarinejad *et al.* 2012; Askarinejad 2013) within the context of the multi-disciplinary research programme on "Triggering of Rapid Mass Movements in steep terrain" (TRAMM). The full-scale field tests were carried out in northern Switzerland in a forested area near Ruedlingen village. The selected experimental site was located on the east-facing bank of the river Rhine, with an average slope angle of approximately 38°. An orthogonal area, with a length of 35m and a width of 7.5m, was instrumented with a wide range of devices.

Figure 1 summarises the geomorphology around the test area with a simplified geological model (Brönnimann *et al.* 2009). The bedrock in the area consists of Molasse formations and includes sandstones and marlstones, deposited with a horizontal layering (Springman *et al.* 2012). Dynamic probing tests around the site revealed uneven bedrock depth, measuring from as deep as 4.5m to as shallow as 0.5m. A network of interconnected fissures running parallel to the river were identified in the bedrock, with openings of several centimetres and filled with soil (Brönnimann *et al.* 2009). These were very effective at draining the overlying colluvium soil cover

(Ruedlingen Soil), which has been characterised as a medium to low plasticity (average PI~10%) silty sand (ML), becoming finer with depth (Casini *et al.* 2010).
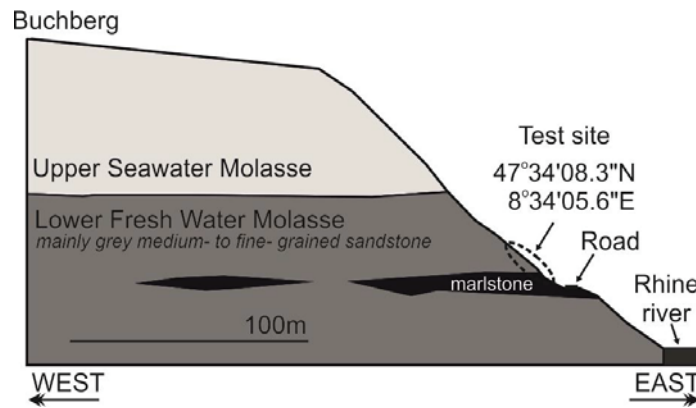

Figure 1. A simplified geological profile of the test area (after Brönnimann *et al.* (2009))

The slope was instrumented extensively to monitor the hydromechanical response during a series of artificial rainfall experiments. The instrumentation plan included earth pressure cells, piezometers, tensiometers, time domain reflectometers (TDRs), acoustic and temperature sensors (Askarinejad 2013). They were installed in three clusters along the slope, as shown in figure 2, and each cluster contained various sensors installed at depth intervals of 0.30m. Slope movements and deformations were monitored both at the surface using photogrammetry, and also within the soil mass by means of novel flexible inclinometers equipped with strain gauges (Askarinejad & Springman 2018).

A first artificial rainfall experiment was executed in October 2008, while the landslide triggering experiment was conducted in March 2009. Building on the results of the first experiment, it was decided to concentrate the sprinklers in the upper part of the experimental area, and to sever the lateral roots along the longitudinal borders of the experimental field down to a maximum depth of 0.4m. The slope was subjected to

artificial rainfall in March 2009, with an average intensity of 20mm/h on the upper part of the slope and 7mm/h in the lower parts.

A significant acceleration in soil movements was observed, approximately 13h after rainfall initiation, which resulted in a generalised slope failure, approximately 2h later. An area measuring 17m (longitudinal) by 7.5m (transversal), with a maximum depth of failure surface of 1.2m, led to a total soil volume of approximately 130m^3 accelerating downslope at an average speed of 0.5 mm/s. The failure was initiated in the upper part of the slope, extending from approximately 5m above cluster 3 down towards, and partly including, cluster 2 (see figure 2). After failure, significant water exfiltration was observed from bedrock fissures within the failed area in the neighbourhood of cluster 3.
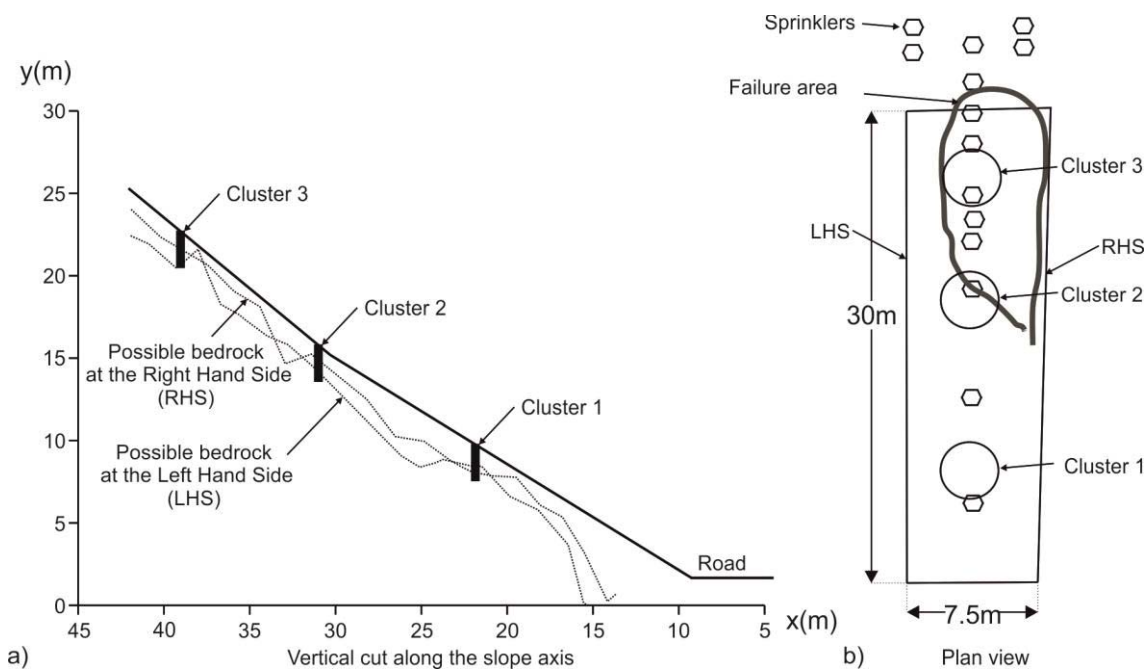

Figure 2. a) The bedrock topography and b) the instrumentation plan (after Askarinejad *et al.* (2010))

3 Constitutive Modelling and Calibration

This section presents and calibrates the main constitutive equations used in the numerical analyses. Starting with the water retention behaviour, Casini (2012) reports a set of degree of saturation vs suction data obtained from remoulded and statically compacted Ruedlingen soil samples. Figure 3 presents the measured data for three different wetting paths, corresponding to different initial void ratio values. The results show the dependence of the water retention behaviour on void ratio, while the sandy nature of the Ruedlingen soil is clearly reflected in the abrupt increase in degree of saturation for suction levels lower than 10kPa.
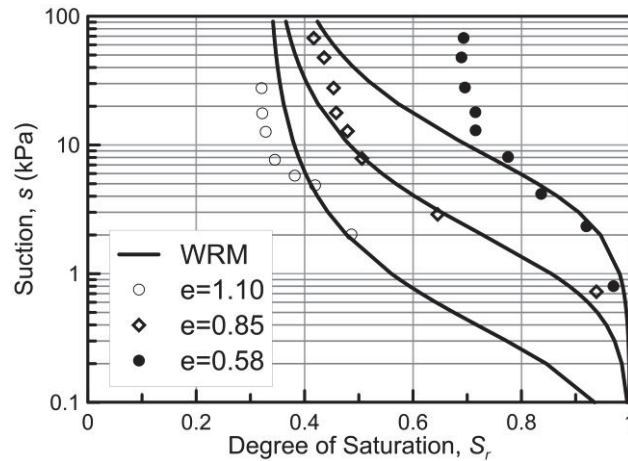

Figure 3. Measured water retention curves (wetting branch) and predictions of the selected WRM according to the selected parameters (table 1) for Ruedlingen Soil

The Van Genuchten (1980) void ratio dependent Water Retention Model (WRM), as implemented in the Code Bright (CB) finite element code, is selected to simulate the water retention behaviour. Water content is described in terms of degree of saturation (S_r) through the following equation:

$$S_r = S_{r,res} + \left(S_{r,max} - S_{r,res}\right)\left[1+\left(\frac{s}{P}\right)^{\frac{1}{1-b}}\right]^{-b} \tag{1}$$

where s is the suction level, b is a model parameter controlling the shape of the reproduced Water Retention Curve (WRC), $S_{r,max}$ and $S_{r,res}$ are the maximum and residual degree of saturation, respectively, and P is a parameter controlling the air-entry value, which is assumed to depend on porosity (n) according to:

$$P = P_0 \cdot \exp(a(n - n_0)) \tag{2}$$

In equation (2), P_0 and n_0 are reference values, and parameter a controls the rate at which parameter P evolves with porosity and in conjunction with void ratio, $e=n/(1 - n)$.

Figure 3 presents the predictions of equations (1) and (2) using the parameters reported in table 1. Note that, following the average in-situ void ratio of Ruedlingen Soil, which is $e=0.9$, calibration has focused on the experimental data corresponding to two soil samples with either $e=0.85$ or $e=1.10$. In a similar manner, given that the initial average suction values measured in the field are in the range of 10kPa, and further considering that the behaviour up to full saturation is of concern, the calibration focuses on capturing the behaviour in the $0.0 \leq s \leq 10$kPa regime.

Table 1. Water retention model parameters for Ruedlingen Soil

Parameter	Value	Parameter	Value
P_0 (kPa)	0.65	a	21.0
b	0.4	n_0	0.47
$S_{r,max}$	1.0	$S_{r,min}$	0.33

The mechanical behaviour is described using the "Clay And Sand Model" (CASM) constitutive model (Yu 1998), which describes the behaviour of clayey and sandy materials in a unified way. Gonzalez (2011) enhanced CASM to account for the

mechanical behaviour of unsaturated soils by incorporating a Loading-Collapse (LC) surface before implementing it in the CB FEM code.

The behaviour is described in terms of Bishop's average skeleton stress (Bishop & Blight 1963):

$$\sigma'_{ij} = \sigma_{ij} - u_a \cdot \delta_{ij} + (u_a - u_w)S_r\delta_{ij} \tag{3}$$

where δ_{ij}=1.0 for $i=j$ and δ_{ij}=0.0 for $i\neq j$, σ_{ij} is the total stress tensor and u_a, u_w are the pressure of the gaseous (air) and the liquid (water) phase, respectively. Suction ($s=u_a-u_w$) is used as the second constitutive variable (Gens 2010). Bishop's average skeleton stress can efficiently represent the non-linear evolution of shear strength with suction (Fredlund *et al.* 1996; Jommi 2000; Alonso *et al.* 2010). A realistic simulation of shear strength evolution plays a fundamental role in the analyses of rainfall induced slope instabilities, as the gradual reduction in shear strength with water infiltration dominates the formation of the failure mechanism.

The CASM yield function, postulated in the triaxial stress space (p', q) takes the following form:

$$f(p',q,p_0(s)) = \left(\frac{q}{M \cdot p'}\right)^{n_c} + \frac{1}{\ln r_c} \cdot \ln \frac{p'}{p_0(s)} \tag{4}$$

where p' is Bishop's mean stress calculated as $p'=p-u_a+S_r \cdot s$ with suction $s=u_a-u_w$, p the mean total stress, q the deviatoric stress and S_r degree of saturation. Variable $p_0(s)$ describes the apparent preconsolidation pressure and controls the size of the yield surface with suction, while parameters n_c and r_c constrain the shape of the yield surface on the deviatoric plane. Inside the yield surface stress states are elastic and straining is described using the Modified Cam Clay (MCC) (Roscoe & Burland 1968) porous-elastic law.

The following equation is adopted to quantify the evolution of the apparent preconsolidation pressure with suction:

$$p_0(s) = p^c \left(\frac{p_0^*}{p^c} \right)^{\frac{\lambda - \kappa}{\lambda(s) - \kappa}}$$

(5)

where p^c is a reference pressure, p_0^* the preconsolidation pressure under saturated conditions that comprises the hardening variable of the model and $\lambda(s)$ the unsaturated compressibility described as:

$$\lambda(s) = \lambda \left[(1-r)e^{-\beta s} + r \right]$$

(6)

In equation (6), β and r are parameters controlling the evolution of compressibility with suction. Note that although equations (5) and (6) are identical to the Barcelona Basic Model (BBM) by Alonso *et al.* (1990), in the "unsaturated" CASM they are used to describe the behaviour in the Bishop's stress domain, which necessitates a different calibration with respect to the BBM. Finally, the CASM model adopts the isotropic volumetric hardening rule of the MCC for the evolution of p_0^* and it incorporates a non-associated flow rule based on Rowe's dilatancy theory (Rowe 1962).

The CASM constitutive model is calibrated for Ruedlingen soil based on an ensemble of experimental results reported in Casini *et al.* (2010), Casini (2012), Casini *et al.* (2013) and Askarinejad (2013), including drained and undrained triaxial compression tests as well as oedometer tests on natural, statically compacted and reconstituted samples of Ruedlingen soil. Various constant water content tests under unsaturated conditions are also reported. Finally, a set of Constant Axial Load (CAL) triaxial tests is also available.

Constant Axial Load (CAL) triaxial tests are performed on anisotropically consolidated soil samples for which the axial load is kept constant following anisotropic compression. The mean effective stress is reduced either by gradually reducing the cell

pressure under unsaturated conditions (Casini *et al.* 2013) or by steadily increasing the pore pressure under a constant cell pressure for saturated samples (Casini *et al.* 2010). Such tests are considered reminiscent of the failure mechanism in slopes subjected to rainfall, where water infiltration leads to an increase in pore pressures under a relatively constant total stress (Anderson & Sitar 1994, Springman *et al.* 2003).

Table 2 summarises the parameters quantified during calibration. The same set of parameters was found capable of accommodating the behaviour of both natural and reconstituted Ruedlingen soil specimens, with exceptions being the slope of the CSL (*M*) and the saturated virgin compressibility (*λ*), where the natural soil samples suggest a slightly higher friction angle and a reduced compressibility. The increased shear strength and reduced compressibility can be indicative of the presence of a structuring agent in the natural soil.

Table 2. Ruedlingen soil: mechanical parameters

Parameter	Value	Parameter	Value
κ	0.01	n_c	1.4
λ	0.09^{*1} -0.13^{*2}	r_c	2.5
v	1/3	p^c (*kPa*)	10
M	$1.2^{*2} - 1.3^{*1}$	β (*MPa^{-1}*)	10000
N_{iso}	$2.21^{*1} - 2.41^{*2}$	r	0.75

[*1] natural soil
[*2] statically compacted

Indicative experimental data for the natural Ruedlingen Soil are compared in figure 4 with numerical results using the CASM model and the parameters taken from table 2

for the natural soil. For the simulations, the initial preconsolidation pressure has been adjusted to the initial void ratio of the specimens, based on the calibrated Isotropic Compression Line (ICL) as described by the following equation:

$$e = (N_{iso} - 1) - \lambda \ln p'$$ (7)

where N_{iso} defines the position of the ICL on the v-lnp' plane and corresponds to the specific volume (v=1+e) under p'=1kPa. The calibrated N_{iso} values are also included in table 2.

The results represent one drained triaxial compression test on an isotropically, normally consolidated soil specimen and two CAL tests following anisotropic consolidation under two different stress obliquities. Accurate simulation of the Ruedlingen soil behaviour during the CAL tests has been prioritised over the isotropically, normally consolidated specimen. The experimental results show in more detail in figure 4(a) that the stress path on the p'−q plane during the CAL phase, slightly overshoots the CSL. "Failure" is manifested by a sudden drop of deviatoric stress, since the specimen cannot sustain the imposed axial load anymore. Numerically, the aforementioned "failure" corresponds to the point where the stress path meets the yield surface (plotted in figure 4(a) for the end of compression) on the dry side of critical state. The increased shape versatility of the CASM yield surface, and especially an independent control of the intersection of the yield surface with the CSL, has proved to be essential in representing "failure" accurately during CAL tests (Sitarenios & Casini 2018). Figures 4(b) & (c) demonstrate that the calibrated CASM model also achieves very good predictions of the compressibility behaviour and of the stress-strain behaviour during triaxial testing.
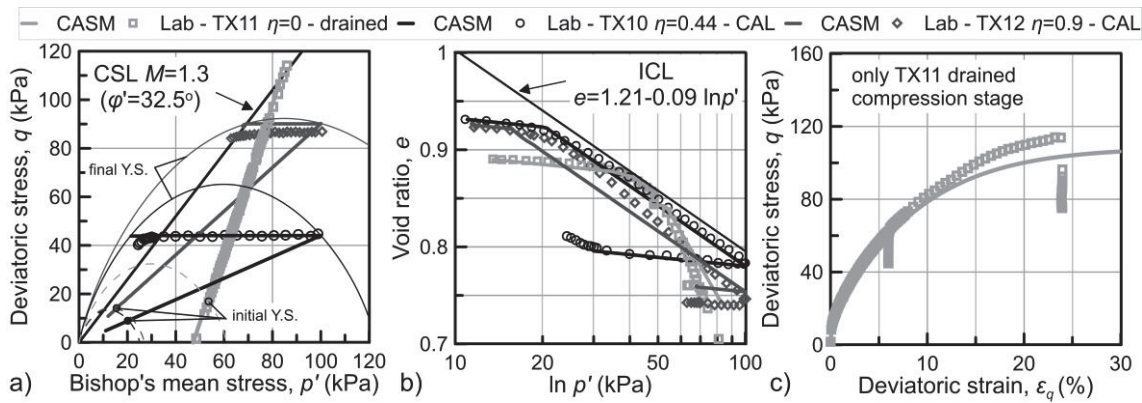
Figure 4. Comparison between data from laboratory tests of isotropic compression - drained compression (TX11) and anisotropic consolidation - constant axial load tests (TX10 & TX12) on saturated natural Ruedlingen specimens; In a) the stress path; b) the volumetric behaviour; c) the stress - strain behaviour, data from Casini *et al.* (2010), and numerical modelling using the CASM model and parameters derived herein

Figure 5 presents similar comparisons for the statically compacted Ruedlingen soil specimens, discussing the behaviour under both saturated and unsaturated conditions. The simulation results cannot capture the strain-softening behaviour exhibited during the undrained triaxial test (TX9) behaviour that is typical of soils with initial anisotropy (Gens 1982); in this particular case (TX9), initial anisotropy can be attributed to the preparation method, which involves 1D static compaction. Although the CASM model includes anisotropic features (e.g., distorted yield surface), it lacks kinematic hardening rules and cannot reproduce intense strain-softening. Nevertheless, the behaviour prior to critical state, which corresponds to failure conditions, is described very satisfactorily. The model captures the shear strength exhibited by the constant water triaxial compression test under unsaturated conditions very well, even though it over-predicts the initial elastic branch. The latter is mainly attributed to the single yield surface, which predicts a large elastic domain, while the end of isotropic compression for the TX5 specimen corresponds to an overconsolidated material state that is still located inside

the yield surface. Finally, like the natural soil, the behaviour is captured very well during constant axial load tests.
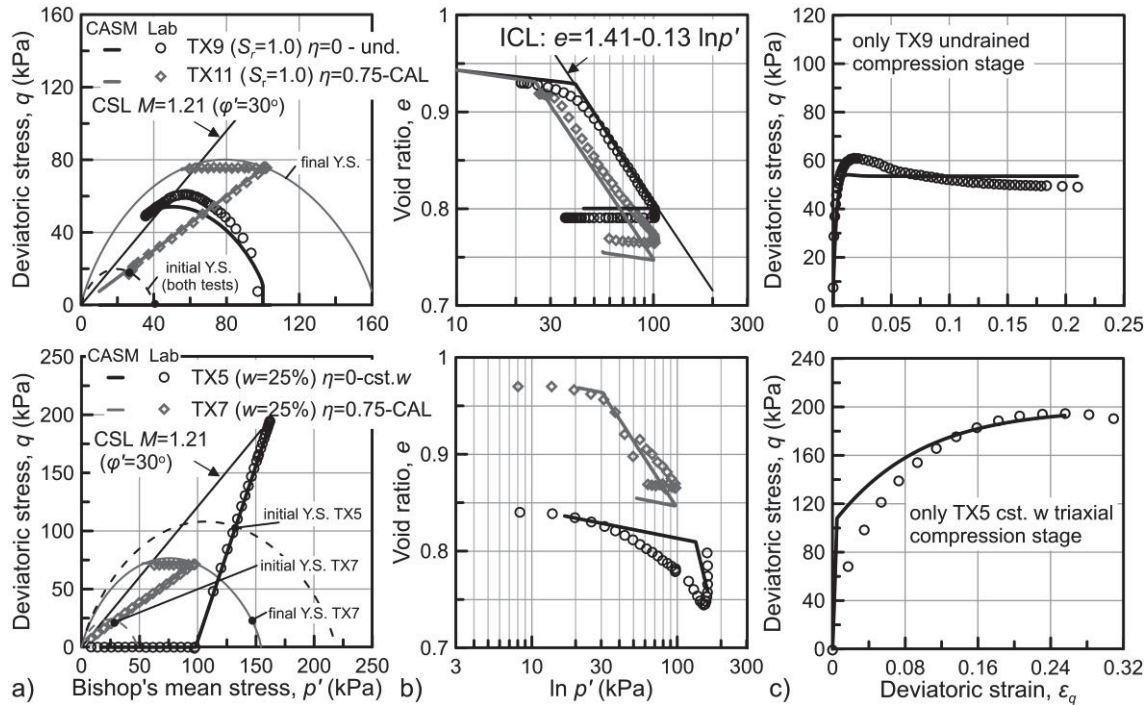

Figure 5. Comparison between data from laboratory tests of isotropic compression - triaxial compression (TX9 & TX5) and anisotropic consolidation - constant axial load tests (TX11 & TX7) on saturated (top) and unsaturated (bottom) statically compacted Ruedlingen samples; In a) the stress path; b) the volumetric behaviour; c) the stress - strain behaviour, data from Casini *et al.* (2013) and numerical modelling using the CASM model and parameters derived herein

4. Simulation of the Landslide Triggering

4.1 Numerical Model Description

Figure 6 presents the 2D, plane strain model adopted for this study. The bedrock is not included in the simulation and suitable mechanical and hydraulic boundary conditions are applied to account for its interaction with the soil cover. The soil-bedrock geometry follows the in-situ determined bedrock depth along the longitudinal vertical section in the middle of the experimental area.

The computational mesh is created with triangular, pore pressure, 6-node, second order finite elements. A dense discretisation is selected with an average element length of 0.25m, resulting in a FEM mesh with 4957 elements and 10482 nodes. The Van-Genuchten WRM and the CASM constitutive model are used to describe the hydromechanical behaviour of the soil. The parameters are reported in tables 1 and 2 respectively, while the mechanical parameters of the natural soil are used in the analyses. Following experimental evidence, the initial void ratio value was set to 0.9. The saturated preconsolidation pressure was selected as 60kPa. It should be highlighted that the value selected deviates from the calibrated compressibility framework, which suggests that for e=0.9, P_0^* is in the order of 30kPa and 50kPa for the natural and the statically compacted material, respectively. However, the selected value was used to prevent accumulation of significant plastic straining during the geostatic step, which could hinder the simulated response during subsequent calculation steps. The air pressure is assumed constant and zero.
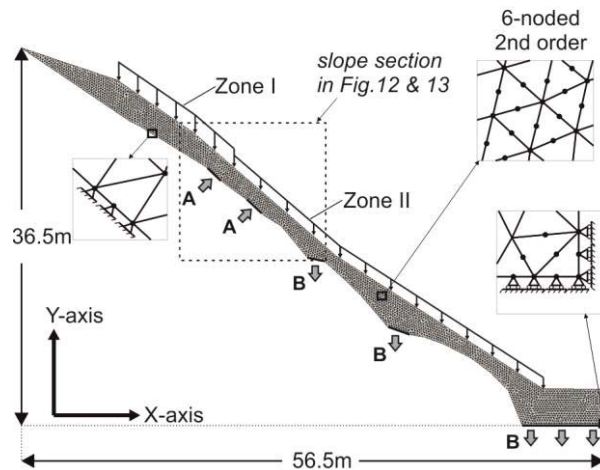

Figure 6. The 2D numerical model in Code Bright

The saturated permeability was set to $k_{sat}=1.0 \cdot 10^{-5}$m/s, which is one order of magnitude higher with respect to the value measured in the laboratory (10^{-6}m/s) by Askarinejad et al. (2012a). It also lies within the range of values determined from in situ

permeability measurements, which suggest values ranging from 10^{-4}m/s to 10^{-5}m/s (Askarinejad 2013; Brönnimann *et al.* 2013). Finally, a typical power law ($k_{rel}=k_{sat}S_r^3$) is selected for the relative unsaturated hydraulic permeability (k_{rel}).

The analysis includes an initial step with duration of 1h, where the soil profile is loaded by gradually increasing gravity. An unsaturated soil profile is simulated from the beginning and the analysis for the initial water equilibrium assumes that the water table coincides with the soil-bedrock interface. The construction phase is followed by a consolidation phase lasting for 50h, at the end of which the hydraulic boundary conditions at the soil-bedrock interface are reconfigured to an impermeable boundary with the exception of three areas, where water is allowed to flow from the soil into the bedrock (B in figure 6). For the latter, suitable seepage boundaries are adopted to allow outflow whenever the pore pressure above becomes positive. This is achieved by selecting a negative leakage coefficient for the flux boundary condition as described in DIT-UPC (2017). They correspond to locations where bedrock fissures, filled with the soil cover, were identified during the geological mapping of the area.

The topography of the simulated slope is steep, which inevitably results in the development of a limited amount of tension stress in some of the elements, mainly at the very top of the slope, where the soil cover depth is shallow (< 0.5m). Critical state models cannot handle tension stresses efficiently as such stress states lie outside the yield surface, while moreover the poroelastic bulk modulus returns a negative value. Consequently, a limited amount of tension strength equal to p_t=4kPa was added to ensure numerical stability. In terms of the Mohr – Coulomb failure envelope and given the simulated friction angle of φ'=32.5° (M=1.3), the applied tension strength corresponds to c'=4·tan32.5°=2.55kPa of cohesion. The applied cohesion is expected to increase the simulated yield locus and strength compared to the calibrated one.

Following the equilibrium step, the artificial rainfall is simulated as a water inflow at the surface of the slope. Rainfall is applied with different intensities at the upper and the lower parts of the slope (Zone I and Zone II in figure 6), representing the rainfall and spatial distribution of the sprinklers during the field experiment (see figure 2). The start of rainfall application is considered as time zero (t = 0h) for the interpretation of the results. Following Askarinejad (2013), the simulated rainfall corresponds to a simplified scenario, which approximates the actual rainfall data, as presented in figure 7. The applied rain intensity is 20mm/h in Zone 1, while it was equal to 7mm/h in Zone 2. Rainfall is applied for 16 hours with a break of 1h between t=2.5h and 3.5h, due to an interruption in the water supply to the sprinklers, which occurred during the field test.
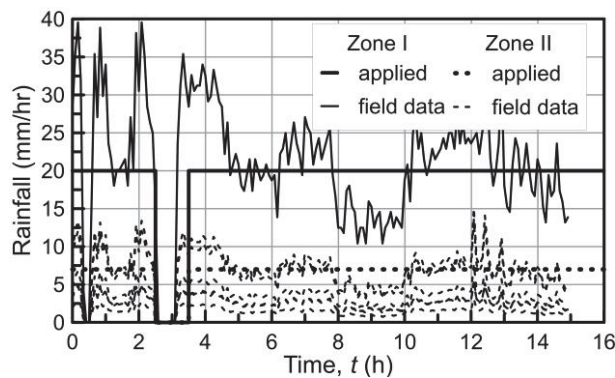

Figure 7. Field rainfall data (from Askarinejad (2013)) and the applied rainfall intensity with time (16/03/2009 12:00 is assumed as t = 0)

Simulation of water exfiltration follows the assumptions made by Askarinejad (2013). The author combined geological information for the potential location of fissures, immediate post-failure observations of profound water exfiltration from the bedrock in cluster 3 and field measurements of pore water pressures (Askarinejad *et al.* 2012b) to conclude that water exfiltration occurs in the upper part of the slope close to cluster 3, as indicated by the arrows with the letter A in figure 6. Moreover, seepage analyses

suggest that the observed hydraulic field can be well approximated by simulating exfiltration as a water inflow with a constant hydraulic head equal to 9kPa, starting 4.5h after rainfall initiation. The same procedure is adopted in this study and the validity of this assumption will be discussed further, based on the numerical results.

4.2 Analysis of Results

Figure 8 presents the distribution of displacements at t=14.4h, which corresponds to the time when the analyses stopped. The displacement field indicates a clear concentration of displacements in the upper part of the slope in the neighbourhood of cluster 3, which suggests that the slope has probably failed. The figure also presents the evolution of displacements with time for selected characteristic points along the slope. Roughly three different behaviour regimes may be identified. An increase in soil movements is observed at t=10h in the central part of the failure area (points C1 to C5) and then displacements increase steadily, initially at a rather constant pace, until an abrupt increase is observed at t=13−14h. The latter is characteristic of unstable behaviour, which explains why the analyses stopped at t=14.5h. It also confirms that the slope had failed physically, as well as in the numerical model.
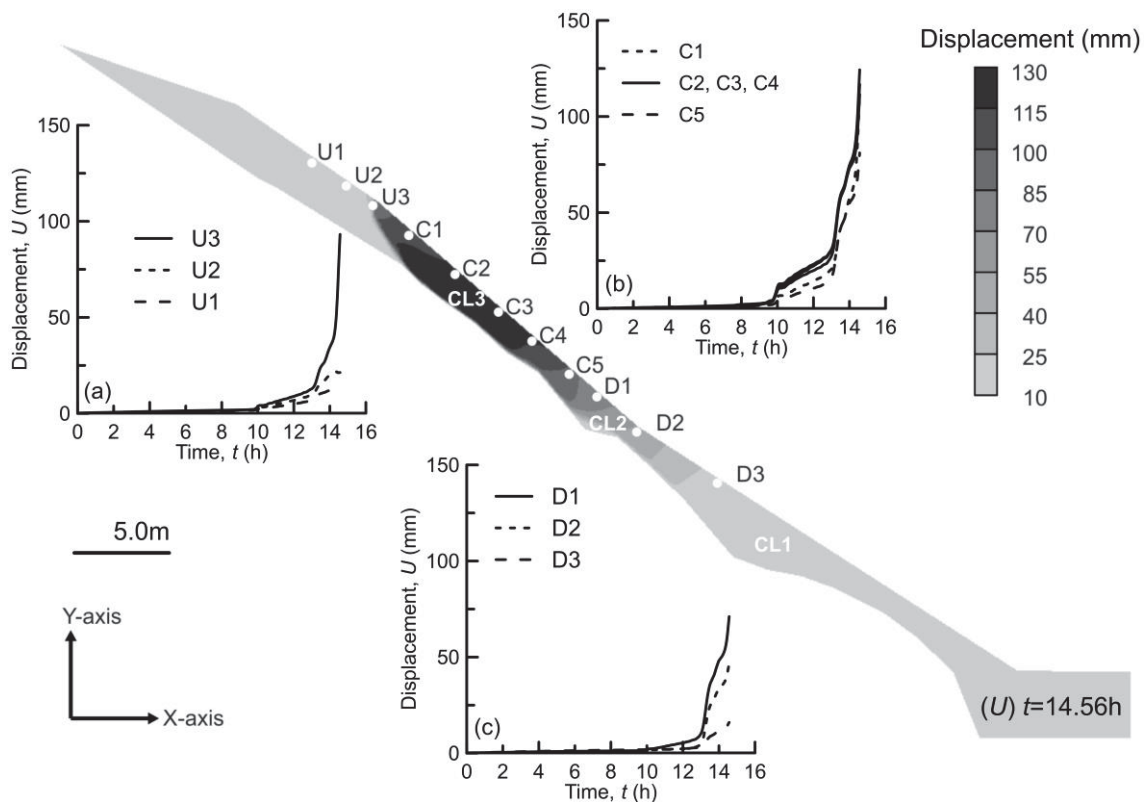
Figure 8. Distribution of displacements at failure (t = 14.56h) and evolution with time for selected locations along the slope

The evolution of displacement shows that failure concentrates in this central area and extends uphill marginally to point U3, while points U1 and U2 are outside the failed soil mass. Downhill, the failure zone extends to point D1, while points D2 and D3 exhibit an increase in displacements only after t=13h, which indicates that they were subject to some form of passive pressure from the uphill failing mass during the latter stages of failure. The predicted failure area compares very well with the field experiment, where failure was observed from approximately 5m above cluster 3 down to cluster 2 (see also figure 2).

Figure 9 focuses on the hydraulic behaviour of the slope. It portrays the distribution of pore water pressure and degree of saturation at failure, together with plots of the

evolution of pore water pressure and of the volumetric water content with time for characteristic points within the three clusters and for equivalent field measurements. Additionally, figure 10 presents and compares with field data the calculated evolution of pore water pressure and of the volumetric water content at two additional depths for cluster 3, one close to the surface (rainfall boundary) and another one deeper, close to the exfiltration boundary, where we can observe a sudden saturation of the soil profile at t=4.5h.

Figures 9 demonstrates a very good match between the numerical and the field data observed along the slope, while figure 10 additionally confirms that the selected simulation of rainfall and water exfiltration provides a fair representation of the observed variation in the hydraulic field with depth, additionally investigating the individual effect of rainfall and exfiltration. The satisfactory comparison confirms and develops further the approach taken in previous studies (Askarinejad et al. 2012; Askarinejad 2013), while validates also the value of permeability selected and calibrates the resulting water retention properties.

The plots in figure 9 clearly suggest that failure happens under fully saturated conditions, while significant pore pressures seem to build up at the soil-bedrock interface in the vicinity of cluster 3, as a result of the applied water exfiltration (see also figure 10). Moreover, a very good match between the measured and the predicted volumetric water content values was observed as failure approached, confirming that values of representative porosity and thus void ratio apply to the soil for the duration of the analyses.
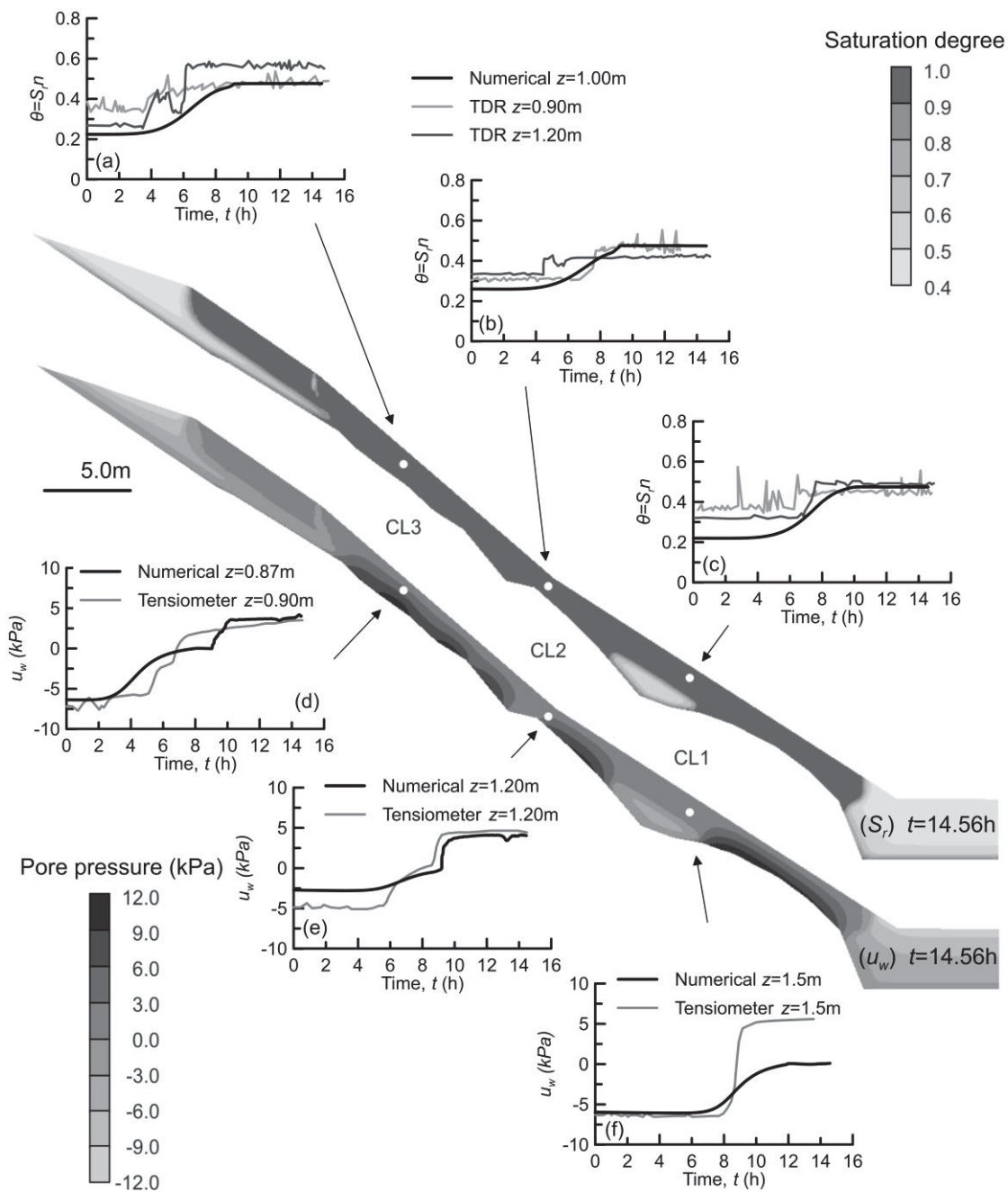
Figure 9. Distribution of pore water pressure and saturation degree at failure together with the evolution at characteristic locations along the slope; field data from Askarinejad (2013)
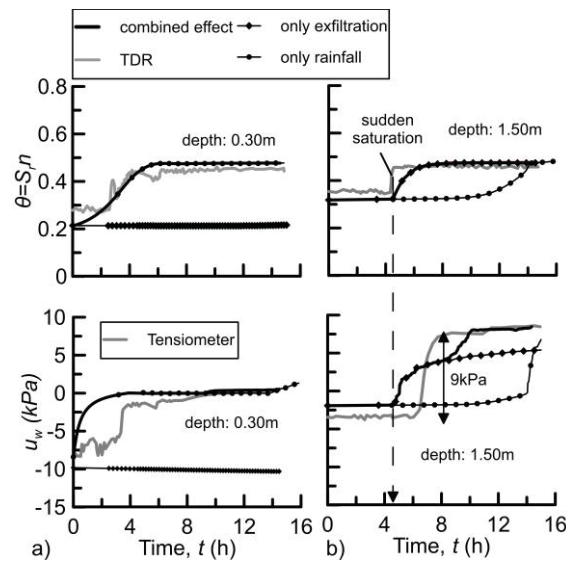
Figure 10. Evolution of volumetric water content (above) and pore water pressure (below) at cluster 3; In a) at a depth of 0.30m and; b) at a depth of 1.5m; for only exfiltration, only rainfall and for their combined effect. Field data from Askarinejad (2013)

Figure 11 concentrates on the displacement field in cluster 3 to examine the slope response leading up to failure. It presents and compares numerical results with displacement measurements from the field. Figure 11(a) compares the vertical displacement of a surface node in cluster 3 with the reported vertical displacement at the same location, the latter, as reported in Askarinejad (2013), based on photogrammetry analyses. Figure 11(b) compares the horizontal displacement of a model node at the depth of 0.5m below the surface, with the reported horizontal displacement of the top of an inclinometer in the same location. A very good match can be seen between the experimental and the numerical results, leading to a very good prediction of the time of failure.

Figures 11(c) and 11(d) plot the evolution of vertical and horizontal velocity with time, corresponding to the numerical results of figures 11(a) and 11(b), respectively. It can

be observed that the slope movements are practically zero for the first 10 hours of rainfall, thereafter both the numerical and the experimental results exhibit the first signs of accumulation of significant displacements. A first notable peak in the velocity is observed in figures 11(c) and 11(d) at the same time (t=10h) with cyclical and smaller peaks in the rate of deformation over the next three hours, when the displacements increase gradually. A second change in the displacement trend is observed, also accompanied with a peak in velocity. Movements accelerate significantly and further displacements occur at an increased velocity, suggesting that t=13h forms a threshold between stable and unstable behaviour. The slope fails, finally, after approximately another 1.5 hours of additional rainfall (t=14.56h).
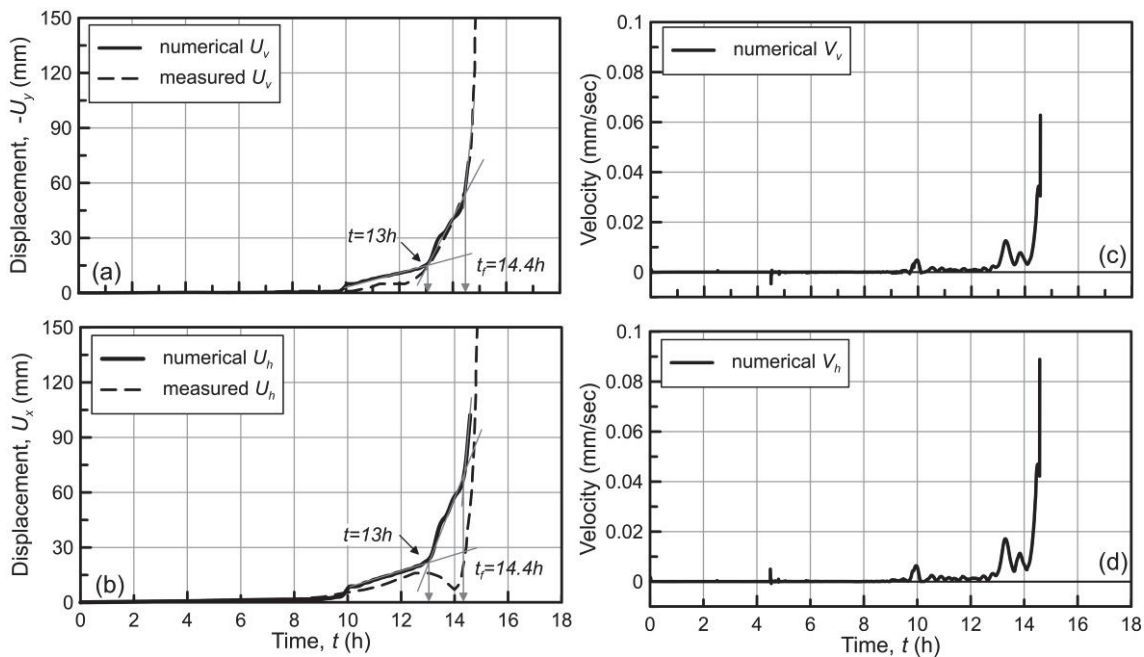

Figure 11. Evolution of displacements (a, b) and velocity (c, d) at the slope surface at cluster 3; field data from Askarinejad (2013)

Timeframes t=10h, 13h and 14.4h correspond to significant "milestones" where the behaviour alters. Figure 12 depicts the distribution of pore pressure, degree of saturation, deviatoric strains and displacements in the area where failure concentrates

for the aforementioned three milestone timeframes. The slope in the failure zone is already saturated at t=10h and in fact, graph (a) in figure 9 suggests that it has just reached (t=9−10h) full saturation. Saturation is attributed to the combined effect of rainfall and water exfiltration from the bedrock. Full saturation results in a significant change in the hydraulic response of the slope as further exfiltration leads to the buildup of positive pore pressures, which cause a significant decrease in shear strength, and hence increasing the necessary mobilised shear strength. The latter is clearly observed as an accumulation of increased deviatoric straining (strain localisation), which for the moment concentrates along the exfiltrating boundaries at the soil-bedrock interface. The observed displacement values are still quite low.

As both exfiltration and rainfall progress, the aforementioned mechanism further increases the plastic strains at the soil-bedrock interface. It seems that this mechanism reaches a threshold at t=13h, where the saturation front has evolved both uphill and downhill, pore pressures have increased further and a region of increased displacements appears at the centre of the area.

Just before the analysis stops at t=14.4h, the distribution of deviatoric strains shows a fully developed failure surface, which has propagated from the soil-bedrock interface towards the surface in the upper part of the slope. The bedrock geometry also plays a role in the exact location of failure surface migration towards the slope surface, as its shape seems to follow a steeper part of the bedrock, as indicated by the small black arrows in figure 12. Contrary to the numerical results, field observations suggest that the slip surface coincides with the soil-bedrock interface only partially and not along the full length of the failed area. Nevertheless, the 2D analyses simulate an average depth of the bedrock, while in reality, the bedrock depth exhibits a significant variation in the transversal direction, which could explain this discrepancy.
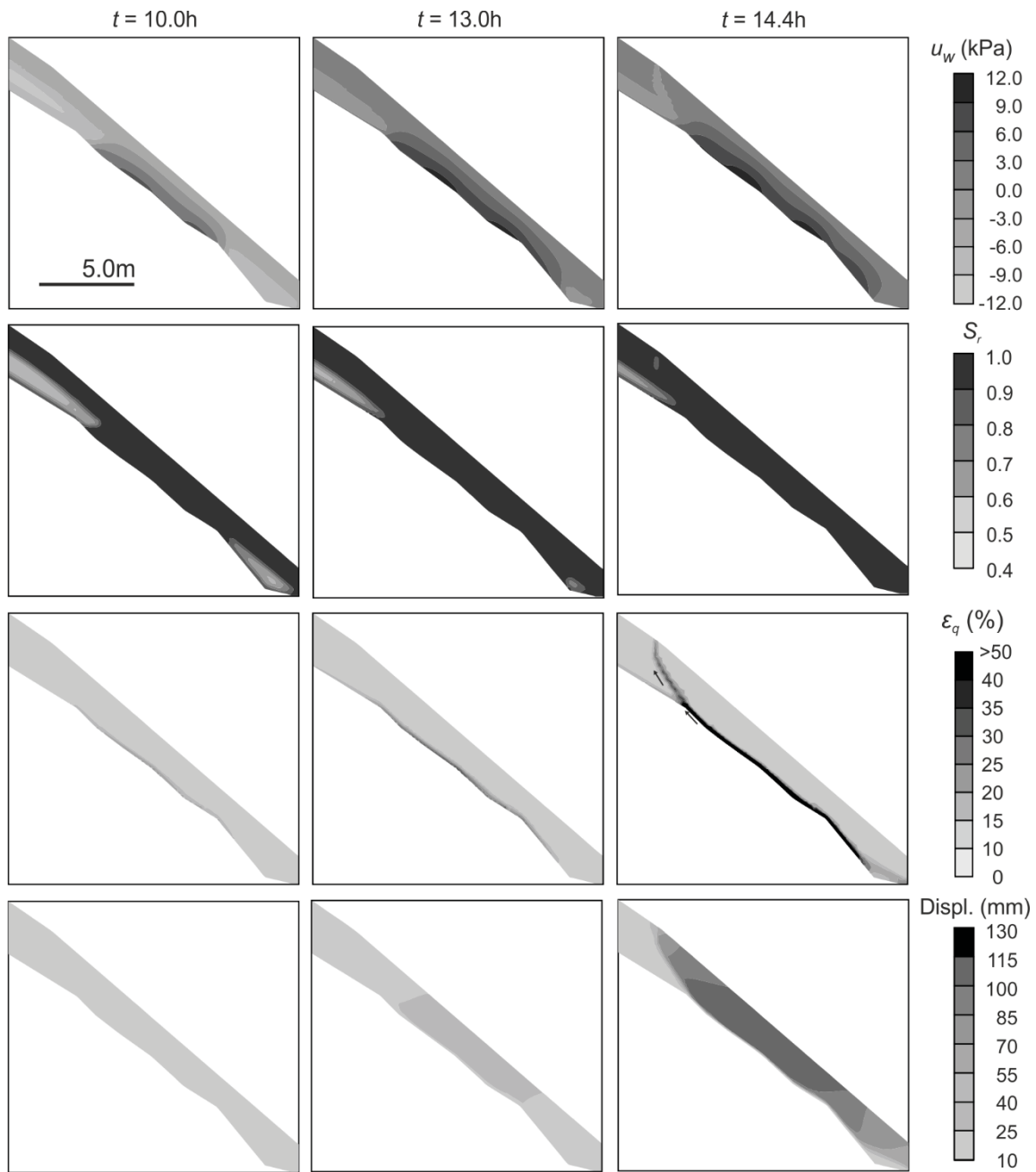
Figure 12. Distribution of pore pressures (u_w), degree of saturation (S_r), deviatoric strains (ε_q) and displacements (U) at three characteristic time frames $t = 10h$, $t = 13h$ and $t = 14.4h$ (slope section as in figure 6)

The distribution of preconsolidation pressure (p_0^*) and void ratio at failure is plotted in Figure 13. The failure surface is well portrayed in both pictures; the final values along the failure surface suggest that the preconsolidation pressure reduces as failure is

approached (initial $p_0{}^*$=60kPa), while at the same time, the void ratio distribution indicates dilatant behaviour (initial e=0.9). The same figure presents the evolution of the stress state, preconsolidation pressure and void ratio with time to explain the behaviour observed, and also combines them as stress path plots in the deviatoric stress ($p'{-}q$) and compressibility ($e{-}p'$) planes. They correspond to a characteristic point in the failure zone along the soil-bedrock interface, which is typical of the behaviour in the failure zone, at the location where exfiltration occurs.
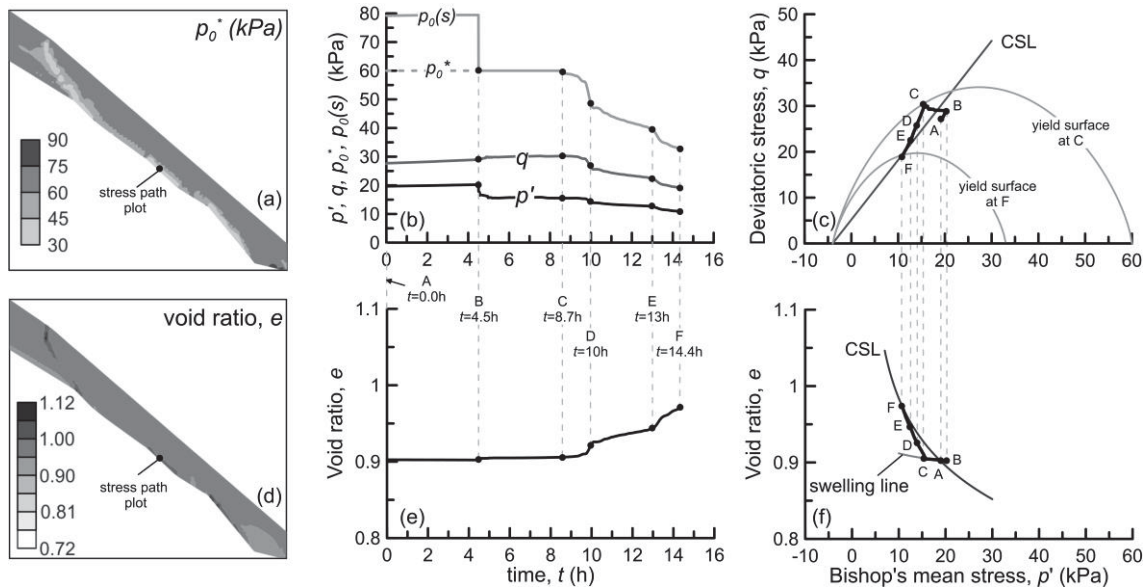

Figure 13. Distribution (slope section as in figure 6) of preconsolidation pressure and void ratio at failure together with the evolution of p', q, $p_0(s)$, $p_0{}^*$ and e

Initially, and until exfiltration is activated (A to B), both p' and q slightly increase following a radial stress path, which is reminiscent of consolidation. This behaviour is the outcome of the progressive saturation of the top soil layers due to rainfall, which increases the bulk unit weight of the soil above the stress path. Exfiltration causes sudden saturation of the soil at the outflow location at t=4.5h, which is reflected as an abrupt drop in the p' value, together with the corresponding abrupt decrease in the apparent preconsolidation pressure, which becomes equal to its saturated counterpart.

This sudden saturation is not accompanied by volumetric collapse as the stress state remains well inside the yield surface.

As rainfall continues and exfiltration progresses, the deviatoric stress slightly increases under a simultaneously reducing p' and the stress path resembles the constant deviator stress path test. This observation further confirms the suitability of the CAL advanced stress path tests in simulating the typical mechanical response of soil elements in rainfall induced slope failures. The behaviour is elastic up to point C (Fig. 13c), so that the soil element reaches the yield envelope at around t=8.5h. The reducing p' results in an increase in the void ratio, with the behaviour plotting on a swelling line (Fig. 13d).

The fact that the yield surface is reached "dry of critical state" ($q > M \cdot p'$) leads to strain softening behaviour, where the size of the yield surface and hence p_0^* decreases and the stress state starts to move towards the failure envelope (CSL). Plastic straining progresses up to failure (point F in Fig.13c, t=14.4h) and is accompanied by a dilative response. A significant amount of plastic straining takes place between t=9h and t=10h, explaining why the first signs of appreciable displacements appear at the slope surface in the same time window. Finally, the stress path has practically reached the failure envelope at t=13h (point E in Fig. 13c), where the majority of the soil elements along the failure surface have almost exhausted the available shear strength (maximum mobilised shear strength), and the slope is on the verge of incipient failure, as has been already discussed with respect to the displacement field.

5 Parametric Study

This section extends the discussion about the Ruedlingen slope behaviour, by examining the effect that different mechanical and hydraulic parameters have on the

numerical response, and mainly on the predicted failure time. The discussion is based on results from an ensemble of additional numerical analyses, where the value of a range of parameters is varied systematically, while the rest of parameters are held constant, as reported in table 2. The results of section 4.2 provide the basis for comparison.

Figure 14 shows the effect of six different mechanical parameters on the predicted evolution of vertical displacement at cluster 3 (similar to figure 10a). In more detail, figures 14(a) to 14(d) focus on plastic behaviour and examine the effect of the preconsolidation pressure p_0^*, virgin (elastoplastic) compressibility λ, elastic compressibility κ and unsaturated compressibility $\lambda(s)$, the latter through parameter r^*. The lower the saturated preconsolidation pressure, the earlier significant plastic deformation initiates, accelerating slope movements and failure. The saturated virgin compressibility has a limited effect on the predicted failure time, whereas an increased elastic compressibility inflates straining and accelerates failure. By evaluating different r^* values, the effect of the unsaturated compressibility framework (LC curve) on the results was investigated and found to be very limited, as the results practically coincide, an additional reflection of the failure mechanism's development under predominantly saturated conditions. Figures 14 (e) and (f) summarise the effect of the failure envelope by examining different slopes (M) of the CSL and different tensile strengths (p_t). As expected, the lower the friction angle or the tensile strength (cohesion), the more rapid the failure and the earlier the time at which the slope starts to exhibit signs of significant movements.
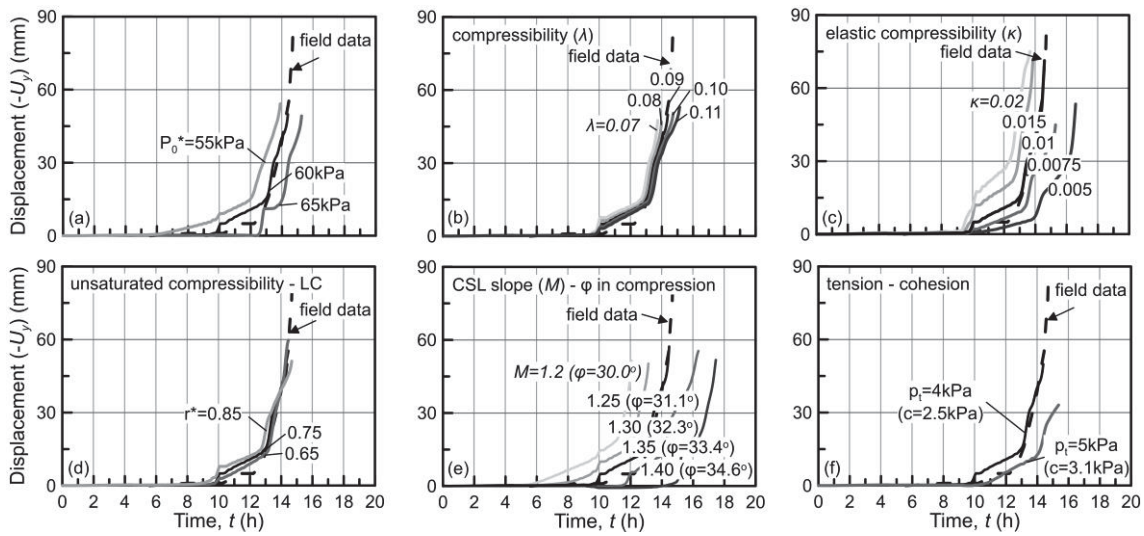
Figure 14. The effect of: a) preconsolidation pressure; b) the saturated virgin compressibility; c) the elastic compressibility; d) the unsaturated compressibility; e) the slope of CSL (friction angle in compression); f) tensile strength (cohesion) on the evolution of displacements at the slope surface in cluster 3.

Figures 15(a) to 15(c) extend the discussion to the effect of the hydraulic parameters and present the vertical displacement, the evolution of pore water pressure and volumetric water content with time, respectively. Five different values of saturated permeability were applied, homogeneously and isotropically, in the soil layer, revealing a dominant effect on the predicted time of failure. Although the values of permeability compared are within the same order of magnitude (10^{-5}m/s), the failure time differs by up to 20 hours. This is directly related to the time required for saturation of the slope close to cluster 3. The higher the permeability, the less time that water infiltrating from precipitation and flowing into the base of the slope from the exfiltration boundaries requires to move through the soil's pores to saturate a substantial portion of the soil cover, thus accelerating failure.
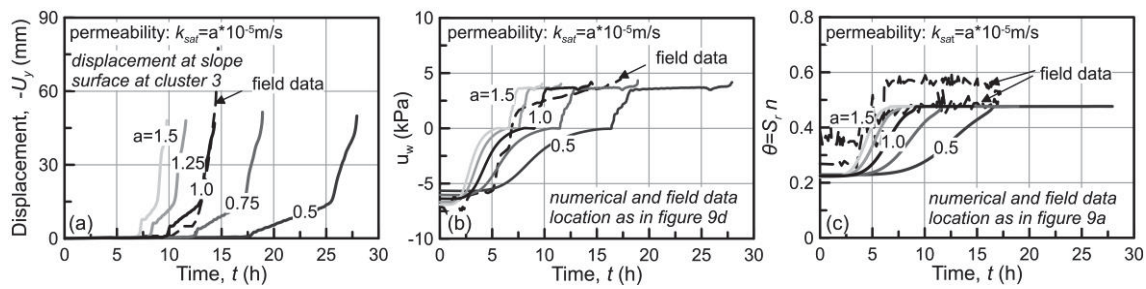
Figure 15. The effect of the saturated hydraulic permeability on: a) the evolution of displacements; b) pore pressure and; c) volumetric water content

Finally, the effect of the soil's capacity for water retention on slope behaviour is depicted in figure 16. The reference analysis, which utilises the void ratio-dependent water retention model (equations (1) and (2)), is compared with the results from three additional analyses based on WRCs I-III, shown in figure 16(a). WRCs I-III are constant void ratio WRCs and correspond to predictions from equations (1) and (2) for initial and constant void ratio values of $e=0.8$ (WRC I), $e=0.9$ (WRC II) and $e=1.0$ (WRC III). The quicker the soil becomes saturated under the critical hydraulic input from rainfall and exfiltration, the earlier failure happens, which occurs first for the lowest void ratio WRC. It is also interesting to observe that the void ratio WRC (reference analysis) in comparison with a fixed WRC under the same initial void ratio (WRC II), shifts the response towards the behaviour of a higher void ratio soil (WRC III). This is another reflection of the soil's dilatant behaviour towards failure, as has been discussed previously.
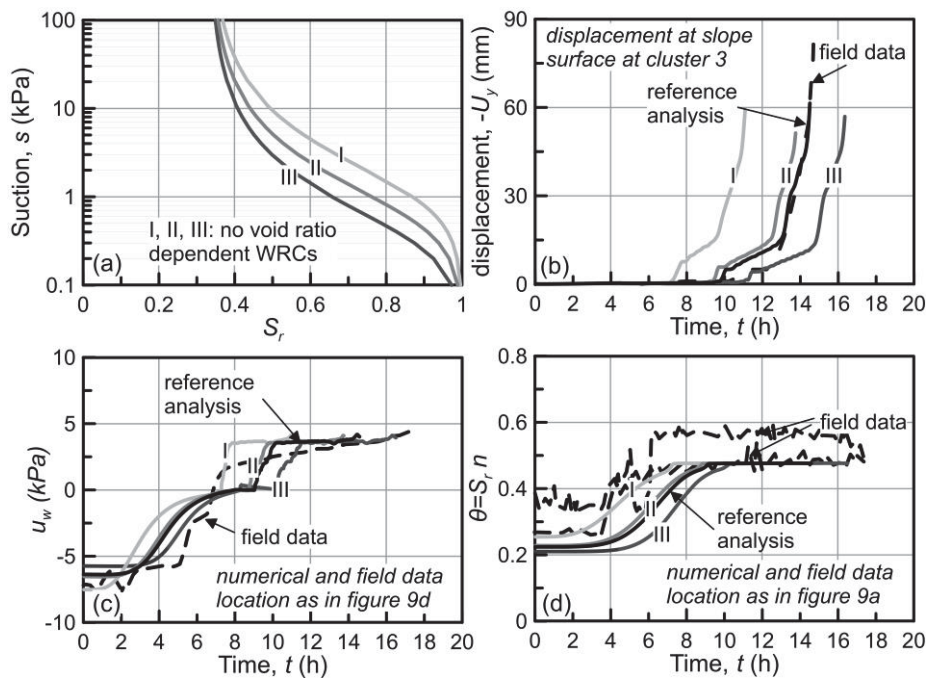
Figure 16. The effect of different water retention behaviour assumptions (a) on: b) the evolution of displacements; c) pore pressure; d) volumetric water content

6 Conclusions

This paper summarises the results of a numerical study based on 2D coupled hydromechanical FEM analyses to simulate an instrumented field experiment, in which a steep forested slope was subjected to intense artificial rainfall. The numerical results were compared with field measurements and very satisfactory agreement was observed, with slope failure occurring approximately fifteen hours after rainfall initiation in both cases. The predicted failure area coincides with the field observations and the evolution of displacements with time was predicted accurately, with the analyses capturing both the initiation of significant straining as well as the abrupt acceleration of movements corresponding to the threshold between stable and unstable behaviour.

A thorough examination of the evolution of both the hydraulic and the mechanical response up to failure revealed that the main triggering agent is the water exfiltration

from the bedrock in the upper part of the slope, which accelerates saturation of the soil cover and increases the pore water pressures above the bedrock. It is attributed to interconnected bedrock fissures, which redirect rainfall water from the upper part of the slope towards emergence locally at lower altitudes. Stress path plots from elements inside the failure surface reveal that most of the elements yield and fail under saturated conditions. Prior to yielding, the stress path is similar to constant axial load (CAL) triaxial tests, confirming the suitability of these experiments in describing the behaviour in slopes subjected to rainfall. Failure is accompanied by dilative response and softening as the stress path towards failure lies on the dry side of the critical state, leading the yield locus to reduce in size. The utilisation of an advanced critical state constitutive model which enables increased versatility of the shape of the yield surface, combined with detailed calibration, plays an important role in the success of the simulation.

Recognising that any calibration and simulation exercise includes a degree of uncertainty and unavoidable numerical assumptions, the paper also includes a parametric investigation into the effect that different mechanical and hydraulic parameters have on the slope response. Note that slightly different set of parameters (i.e., lower strength combined with lower permeability) can perhaps capture aspects of the observed behaviour equally well. However, reasonable variations in the hydraulic and mechanical parameters do not alter fundamental aspects of the suggested triggering procedure and failure mechanism. Future research will attempt to account for additional refinements such as 3D analyses, the effect of the bedrock inclination in the transversal direction, any effects of roots on the hydraulic and mechanical regimes near to the surface and a more detailed study of the various assumptions related to the exfiltration, which was identified as the key to the slope failure.

Acknowledgements

References

Alonso, E. E., Gens, A. & Josa, A. (1990). A constitutive model for partially saturated soils. *Géotechnique* **40**, No. 3, 405–430.

Alonso, E. E., Pereira, J.-M., Vaunat, J. & Olivella, S. (2010). A microstructurally based effective stress for unsaturated soils. *Géotechnique* **60**, No. 12, 913–925.

Anderson, S. & Sitar, N. (1994). Procedures for analysis of the mobilization of debris flows. In *Proc. of the International Conference on Soil Mechanics and Foundation Engineering - International Society for Soil Mechanics and Foundation Engineering*, vol. 1, AA BALKEMA, pp. 255–255.

Askarinejad, A. (2013). *Failure mechanisms in unsaturated silty sand slopes triggered by rainfall*. D.Sc. thesis, ETH Zurich, doi:10.3218/3677-0.

Askarinejad, A., Akca, D. & Springman, S. M. (2018). Precursors of instability in a natural slope due to rainfall: a full-scale experiment. *Landslides* **15**, No.9, 1745 - 1759.

Askarinejad, A., Beck, A., Casini, F. & Springman, S. M. (2012a). Unsaturated hydraulic conductivity of a silty sand with the instantaneous profile method. In *E-Unsat 2012, Unsaturated soil: research and applications*, Naples, Italy, 2:215-220.

Askarinejad, A., Casini, F., Bischof, P., Beck, A. & Springman, S. M. (2012b). Rainfall induced instabilities: a field experiment on a silty sand slope in northern Switzerland. *Italian Geotechnical J. (RIG)* **3**, No. 12, 50–71.

Askarinejad, A., Casini, F., Kienzler, P., Teysseire, P. & Springman, S. (2010). Mountain risks: two case histories of landslides induced by artificial rainfall on steep slopes. In *Proc. International Conference on Mountain risks: bringing science to society*, Florence, Italy. pp. 201–206.

Askarinejad, A., Laue, J. & Springman, S.M. (2014). Effect of bedrock shape and drainage properties on the stability of slopes. In *Proc. International Conference on Physical Modelling in Geotechnics (ICPMG 2014), Perth* 2, 1211–1217.

Askarinejad, A. & Springman, S. M. (2018). A novel technique to monitor subsurface movements of landslides. *Canadian Geotechnical J.* **55**, No. 5, 620–630.

Bishop, A. W. & Blight, G.E. (1963). Some aspects of effective stress in saturated and partly saturated soils. *Géotechnique* **13**, No. 3, 177-197.

Brönnimann, C., Stähli, M., Schneider, P., Seward, L. & Springman, S. M. (2013). Bedrock exfiltration as a triggering mechanism for shallow landslides. J. *Water Resources Res.* **49**, No. 9, 5155–5167.

Brönnimann, C., Tacher, L., Askarinejad, A., Kienzler, P. & Springman, S. (2009). Porewater pressure modelling in a rainfall triggered shallow landslide: the sprinkling experiment in Ruedlingen, Canton of Schaffhausen. In *Proc. 7th Swiss Geoscience Meeting*, Neuchâtel, Switzerland.

Caine, N. (1980). The rainfall intensity-duration control of shallow landslides and debris flows. *Geografiska Annaler* **62A**, 23–27.

Cascini, L., Cuomo, S. & Guida, D. (2008). Typical source areas of May 1998 flow-like mass movements in the Campania region, Southern Italy. *Engng Geol.* **96**, No. 3-4, 107–125.

Casini, F. (2012). Deformation induced by wetting: a simple model. *Canadian Geotechnical J.* **49**, No. 8, 954–960.

Casini, F., Jommi, C. & Springman, S. (2010). A laboratory investigation on an undisturbed silty sand from a slope prone to landsliding. *Granular Matter* **12**, No. 3, 303–316.

Casini, F., Serri, V. & Springman, S. (2013). Hydromechanical behaviour of a silty sand from a steep slope triggered by artificial rainfall: from unsaturated to saturated conditions. *Canadian Geotechnical J.* **50**, No. 1, 28–40.

Damiano, E., Greco, R., Guida, A., Olivares, L. & Picarelli, L. (2017). Investigation on rainwater infiltration into layered shallow covers in pyroclastic soils and its effect on slope stability. *Engng. Geol.* **220**, 208–218.

DIT-UPC (2017). CODE_BRIGHT, a 3-D program for thermohydro-mechanical analysis in geological media: User's guide. Barcelona: Centro Internacional de Métodos Numéricos en Ingeniería (CIMNE).

Elia, G., Cotecchia, F., Pedone, G., Vaunat, J., Vardon, P. J., Pereira, C., Springman, S. M., Rouainia, M., Van Esch, J., Koda, E., Josifovski, J., Nocilla, A., Askarinejad, A., Stirling, R., Helm, P., Lollino and Osinski, P. (2017). Numerical modelling of slope–vegetation–atmosphere interaction: an overview. *Quart. J. Engng. Geol. and Hydrogeol.* **50**, No. 3, 249–270.

Fredlund, D. G., Xing, A., Fredlund, M. D. & Barbour, S. (1996). The relationship of the unsaturated soil shear to the soil-water characteristic curve. *Canadian Geotechnical J.* **33**, No. 3, 440–448.

Gens, A. (1982). *Stress-strain and strength characteristics of a low plasticity clay*. Ph.D. thesis, Imperial College London.

Gens, A. (2010). Soil–environment interactions in geotechnical engineering. *Géotechnique* **60**, No. 1, 3–74.

Gonzalez, N. (2011). *Development of a family of constitutive models for geotechnical applications*. Ph.D. thesis, Universitat Politécnica de Catalunya.

Guzzetti, F., Cardinali, M., Reichenbach, P., Cipolla, F., Sebastiani, C., Galli, M. & Salvati, P. (2004). Landslides triggered by the 23 November 2000 rainfall event in the Imperia province, Western Liguria, Italy. *Engng. Geol.* **73**, No. 3-4, 229–245.

Harp, E. L., Wells, W. G. & Sarmiento, J. G. (1990). Pore pressure response during failure in soils. *Geol. Soc. America Bull.* **102**, No. 4, 428–438.

Jommi, C. (2000). Remarks on the constitutive modelling of unsaturated soils. In *Experimental evidence and theoretical approaches in unsaturated soils: Proceedings, international workshop on unsaturated soils, Trento,* 139–153.

Laloui, L., Ferrari, A., Li, C. & Eichenberger, J. (2015). Hydro-mechanical analysis of volcanic ash slopes during rainfall. *Géotechnique* **66**, No. 3, 220–231.

Lehmann, P., Gambazzi, F., Suski, B., Baron, L., Askarinejad, A., Springman, S. M., Holliger, K. & Or, D. (2013). Evolution of soil wetting patterns preceding a hydrologically induced landslide inferred from electrical resistivity survey and point measurements of volumetric water content and pore water pressure. *J. Water Resources Res.* **49**, No. 12, 7992–8004.

Leroueil, S. (2001). Natural slopes and cuts: movement and failure mechanisms. *Géotechnique* **51**, No. 3, 197–243.

Lollino, P., Cotecchia, F., Elia, G., Mitaritonna, G. & Santaloia, F. (2016). Interpretation of landslide mechanisms based on numerical modelling: two case-histories. *Eur. J. of Environ. and Civil Engng.* **20**, No. 9, 1032–1053.

Ng, C. W., Wang, B. & Tung, Y.-K. (2001). Three-dimensional numerical investigations of groundwater responses in an unsaturated slope subjected to various rainfall patterns. *Canadian Geotechnical J.* **38**, No. 5, 1049–1062.

Ochiai, H., Okada, Y., Furuya, G., Okura, Y., Matsui, T., Sammori, T., Terajima, T. & Sassa, K. (2004). A fluidized landslide on a natural slope by artificial rainfall. *Landslides* **1**, No. 3, 211–219.

Olivella, S., Gens, A., Carrera, J. & Alonso, E. (1996). Numerical formulation for a simulator (Code Bright) for the coupled analysis of saline media. *Engng. Comp.* **13**, No. 7, 87–112.

Rahardjo, H., Ong, T., Rezaur, R. & Leong, E. C. (2007). Factors controlling instability of homogeneous soil slopes under rainfall. *J. Geotech. and Geoenviron. Engng.* **133**, No. 12, 1532–1543.

Rickli, C., H. Raetzo, B. McArdell, and J. Presler (2008), Hanginstabilitäten, In *Ereignisanalyse Hochwasser 2005 Teil 2 Analyse von Prozessen, Massnahmen und Gefahrengrundlagen, edited by G.R. Bezzola, and C. Hegg, pp. 84, Bundesamt für Umwelt BAFU, Bern und der Eidgenössischen Forschungsanstalt für Wald, Schnee und Landschaft WSL, Birmensdorf, Switzerland.*

Roscoe, K. & Burland, J. (1968). On the generalized stress strain behaviour of 'wet' clay. In *Engineering Plasticity* (Heyman J., Leckie F. (eds)) Cambridge: Cambridge University Press, pp. 535-608.

Rowe, P. W. (1962). The stress dilatancy relation for static equilibrium of an assembly of particles in contact. *Proc. R. Soc. A* **269**, 500–527.

Salciarini, D., Tamagnini, C., Conversini, P. & Rapinesi, S. (2012). Spatially distributed rainfall thresholds for the initiation of shallow landslides. *Natural Hazards* **61**, No. 1, 229–245.

Sitarenios, P. & Casini, F. (2018). Evaluating different yield surface assumptions in representing constant axial load tests which follow anisotropic consolidation. *In Proc. of the 7th International Conference on Unsaturated Soils, Hong Kong, China, 3-5 Aug. 2018.*

Springman, S. M., Jommi, C. & Teysseire, P. (2003). Instabilities on moraine slopes induced by loss of suction: a case history. *Géotechnique* **53**, No. 1, 3–10.

Springman, S. M., Askarinejad, A., Casini, F., Friedel, S., Kienzler, P., Teysseire, P. & Thielen, A. (2012). Lessons learnt from field tests in some potentially unstable slopes in Switzerland. *Acta Geotechnica Slovenica* **1**, 5–29.

Take, W. A., Bolton, M. D., Wong, P. C. P. & Yeung, F. J. (2004). Evaluation of landslide triggering mechanisms in model fill slopes. *Landslides* **1**: 173-184.

Tang, A.-M., Askarinejad, A., Cui, Y. J., Gentile, F., Gowing, J., Jommi, C., Kehagia, F., Keszeyné Say, E., ter Maat, H. W., Lenart, S., Lourenco, S., Oliveira, M., Osinski, P., Springman, S. M., Stirling, R., Toll, D. & Viterbo, p. (2018). Atmosphere–vegetation–soil interaction impacts on engineered slopes: A review on recent advances. *Quart. J. Engng. Geol. and Hydrogeol.* **51**, No. 2: 156-168, doi: http://dx.doi.org/10.1144/qjegh2017-103.

Van Genuchten, M. T. (1980). A closed-form equation for predicting the hydraulic conductivity of unsaturated soils 1. *Soil Sci. Soc. America J.* **44**, No. 5, 892–898.

Wang, G. & Sassa, K. (2003). Pore-pressure generation and movement of rainfall-induced landslides: effects of grain size and fine-particle content. *Engng. Geol.* **69**, No. 1-2, 109–125.

Wu, L., Huang, R., Xu, Q., Zhang, L. & Li, H. (2015). Analysis of physical testing of rainfall induced soil slope failures. *Environ. Earth Sci.* **73**, No. 12, 8519–8531.

Yu, H.-S. (1998). CASM: A unified state parameter model for clay and sand. *Int. J. Num. and Anal. Meth. Geomech.* **22**, No. 8, 621–653.

Figure captions

Figure 1. A simplified geological profile of the test area (after Brönnimann *et al.* (2009))

Figure 2. a) The bedrock topography and b) the instrumentation plan (after Askarinejad *et al.* (2010))

Figure 3. Measured water retention curves (wetting branch) and predictions of the selected WRM according to the selected parameters (table 1) for Ruedlingen Soil

Figure 4. Comparison between data from laboratory tests of isotropic compression - drained compression (TX11) and anisotropic consolidation - constant axial load tests (TX10 & TX12) on saturated natural Ruedlingen specimens; In a) the stress path; b) the volumetric behaviour; c) the stress - strain behaviour, data from Casini *et al.* (2010), and numerical modelling using the CASM model and parameters derived herein

Figure 5. Comparison between data from laboratory tests of isotropic compression - triaxial compression (TX9 & TX5) and anisotropic consolidation - constant axial load tests (TX11 & TX7) on saturated (top) and unsaturated (bottom) statically compacted Ruedlingen samples; In a) the stress path; b) the volumetric behaviour; c) the stress - strain behaviour, data from Casini *et al.* (2013) and numerical modelling using the CASM model and parameters derived herein

Figure 6. The 2D numerical model in Code Bright

Figure 7. Field rainfall data (from Askarinejad (2013)) and the applied rainfall intensity with time (16/03/2009 12:00 is assumed as $t = 0$)

Figure 8. Distribution of displacements at failure ($t = 14.56h$) and evolution with time for selected locations along the slope

Figure 9. Distribution of pore water pressure and saturation degree at failure together with the evolution at characteristic locations along the slope; field data from Askarinejad (2013)

Figure 10. Evolution of volumetric water content (above) and pore water pressure (below) at cluster 3; In a) at a depth of 0.30m and; b) at a depth of 1.5m; for only exfiltration, only rainfall and for their combined effect. Field data from Askarinejad (2013)

Figure 11. Evolution of displacements (a, b) and velocity (c, d) at the slope surface at cluster 3; field data from Askarinejad (2013)

Figure 12. Distribution of pore pressures (u_w), degree of saturation (S_r), deviatoric strains (ε_q) and displacements (U) at three characteristic time frames $t = 10h$, $t = 13h$ and $t = 14.4h$ (slope section as in figure 6)

Figure 13. Distribution (slope section as in figure 6) of preconsolidation pressure and void ratio at failure together with the evolution of p', q, $p_0(s)$, p_0^* and e

Figure 14. The effect of: a) preconsolidation pressure; b) the saturated virgin compressibility; c) the elastic compressibility; d) the unsaturated compressibility; e) the slope of CSL (friction angle in compression); f) tensile strength (cohesion) on the evolution of displacements at the slope surface in cluster 3.

Figure 15. The effect of the saturated hydraulic permeability on: a) the evolution of displacements; b) pore pressure and; c) volumetric water content

Figure 16. The effect of different water retention behaviour assumptions (a) on: b) the evolution of displacements; c) pore pressure; d) volumetric water content

Table captions

Table 1. Water retention model parameters for Ruedlingen Soil

Table 2. Ruedlingen soil: mechanical parameters